Comparison of error correction codes via optimal channel replay of high north underwater acoustic channels

Konstantinos Pelekanakis [a],[*], Pietro Paglierani [b], Alberto Alvarez [b], João Alves [b]

[a] *Netherlands Organisation for Applied Scientific Research (TNO), The Hague, NL-2597 AK, The Netherlands*
[b] *Centre for Maritime Research and Experimentation (CMRE), La Spezia, 19126, Italy*

ARTICLE INFO

ABSTRACT

This paper aims to enhance the reliability of underwater acoustic (UWA) communications by evaluating the effectiveness of various Forward Error Correction (FEC) codes. In the absence of standardized UWA physical layer simulators, we rely on in-situ data to assess the performance of six FEC codes: convolutional, turbo, Low-Density Parity Check (LDPC), Bose– Chaudhuri–Hocquenghem (BCH), Turbo Product Code (TPC), and polar. We examine two common payload sizes: 128-bit packets at a 1/5 encoding rate and 1024-bit packets at a 1/2 rate. Our comparative analysis leverages previously recorded single-carrier Phase-Shift Keying (PSK) signals, originally not intended for FEC evaluation. The signals were transmitted over various underwater links in a High North environment, including areas of sea surface ice floes, northwest of the Svalbard Islands. Using these signals, we formulate an optimal channel replay framework for FEC comparison through constellation dithering for M-ary PSK (M-PSK) modulation. This framework involves a Channel Estimate-Based-Decision Feedback Equalizer (CEB-DFE) with a varying number of input channels (hydrophones) at the receiver end. We focus on the Packet Error Rate (PER), maintaining consistent channel conditions for all codes under consideration. The polar code demonstrates the best performance by achieving the lowest PER for all tested packet lengths and varying number of hydrophones. Moreover, upgrading the equalizer with a turbo feature enables the polar code to achieve up to a 45% further reduction in PER in certain scenarios.

1. Introduction

The "High North", the water body situated above 80° latitude, has become increasingly significant in the domain of underwater acoustic (UWA) communications due to its rapid transformation catalyzed by climate change [1]. As highlighted by the Intergovernmental Panel on Climate Change (IPCC), this region has been experiencing warming approximately twice the global average since the 1980s [2]. Climate forecasts suggest that the Arctic will experience an ice-free summer by mid-century [3]. Moreover, inflows of fresh water from sea ice melt, glacier runoff, and northern rivers are expected to rise by 30% at that period [4]. As the perennial sea ice canopy dwindles, UWA signals interacting with sea surface may experience reduced scattering losses. However, this also means that ambient noise may not be as effectively dampened. Moreover, while the noise resulting from ice activities like fracturing, rafting, and ridging will decrease, the emergence of new open water areas may enhance the ambient noise-induced by wind and rain.

In addition to the evolving scattering conditions resulting from the ice canopy's thawing, refraction effects related to water column stratification play a pivotal role in sound propagation. Research in the High North indicates a potential shift from the traditional stratification, where salinity uniformly escalates with depth, to a more complex layering structure. In this new structure, elevated temperatures necessitate reversals in salinity gradients. Notably, sharp fluctuations in these gradients can emerge along the pycnocline (spiciness effect), even in the absence of horizontal gradients [5]. The generation of a warmer and long-lasting near-surface layer with a temperature maximum as well as intrusions of warm Pacific (American Arctic) and Atlantic (European Arctic) waters generate sound ducting in the surface mixed layer (SML) [6,7]. During the last decade, a sound duct has prominently appeared in the Beaufort Sea (refereed to as Beaufort Lens) enabling acoustic propagation distances exceeding 400 km [8].

The limited experimentation with UWA communication systems in the High North has left gaps in our understanding of how these systems can be efficiently used in this region. Current systems are based on well-known *diversity* techniques to mitigate signal fading and ambient noise. Systems exploiting *explicit* diversity are described in [9–11], where the information bits are encoded with convolutional codes and the

* Corresponding author.
   E-mail address: costas.pelekanakis@tno.nl (K. Pelekanakis).

resulting coded bits are time-scrambled and transmitted over different tones via Frequency-Shift Key (FSK) modulation. The receiver leverages on the fact that each transmitted codeword experiences uncorrelated time-frequency fading to improve the reliability of the link. Systems exploiting *implicit* diversity are described in [9,10,12–15], where the data bits are encoded with a convolutional encoder and the resulting coded bits are time-scrambled and modulated via single-carrier Phase-shift keying (PSK). Since the transmitted codeword occupies the entire frequency band, it grants the potential to the Decision Feedback Equalizer (DFE) receiver to mitigate frequency-selective fading. Additional reliability gain has been demonstrated when the DFE coherently combines signals arriving at spatially-separated hydrophones.

All the above-mentioned Arctic communications systems use Forward Error Correction (FEC) by means of convolutional codes. The popularity of convolutional codes is mainly because they can be designed with various code rates (the ratio of input bits to encoded bits) and constraint lengths, allowing for flexibility in meeting specific application requirements. However, convolutional codes is one FEC technique among many alternatives. For example, the UWA community has tested various types of FEC codes in communication systems operating at mid-latitude environments. Reed Solomon and Bose–Chaudhuri–Hocquengham (BCH) codes have been studied, respectively, in [16, 17]. Capacity-achieving codes[1] such as turbo [18–20], Low-Density Parity Check (LDPC) [21,22] and polar [23,24] have been successfully demonstrated during the last 15 years.

Despite the studies addressing FEC performance, there is very limited work in comparing the performance of different FEC codes in similar experimental UWA channels. Performance rankings provide valuable insights into the strengths and weaknesses of different codes, aiding in the selection of the most appropriate coding scheme for a given link and operational resources (bandwidth, power, computational complexity, delay requirements, to name a few). In addition, performance rankings play a crucial role in standardization efforts; standardization bodies consider the performance rankings of error-correcting codes when defining communication standards. To the best of our knowledge, only the papers [17,24,25] compare different FEC codes in the same experimental channels. In particular, Trellis-coded Modulation (TCM) was compared against Bit-Interleaved Coded Modulation (BICM) off the coast of Narragansett Bay at Rhode Island, USA, [25], BCH was compared against convolutional and turbo codes in the South Sea of Korea [17] and polar was compared against LDPC at the Qiandao Lake in China [24].

The contribution of this work, which is an extension of the WUWNet 2022 conference paper [26], aims to pave the way for more efficient and robust UWA communication systems in challenging environments. A key development is the creation of a specialized channel replay framework tailored for the multi-channel DFE. This framework allows for a direct comparison of various FEC codes under identical conditions, including multipath and noise. In particular, we compare the performance of convolutional, turbo, LDPC, Turbo Product Code (TPC), BCH, and polar code under an equal coding rate constraint. Moreover, the comparison utilizes real data from a previous at-sea experiment conducted northwest off the Svalbard Islands. An in-depth performance analysis in relation to the number of hydrophones used at the receiver is carried out. Finally, the study delves into the performance impact of integrating turbo equalization at the receiver's front-end, providing insights into the enhancement of communication system efficacy.

The paper is structured as follows. In Section 2, we introduce the proposed dithering framework for coded modulation based on M-PSK constellations. Section 3 describes the considered channel codes. In Section 4, we present the collection of experimental data and discuss relevant acoustic channel conditions. In Section 5, the error rate comparison of the six codes is presented. Section 6 concludes our work.

---

[1] These codes have the property to achieve channel capacity of the additive white Gaussian noise (AWGN) channel as the codeword increases.

2. Optimal channel replay framework for constant modulus constellations

Channel replay is a technique to emulate the performance of a communication system using channels collected during a previous at-sea experiment. The emulated system output resembles real-life performance, faithfully replicating channel-induced signal distortions encountered during the experimental phase. While the replay bit rate can be adjusted as a flexible parameter, it is important to note that the replay band is bounded by the one employed during the experiment. For the ubiquitous class of linear modulation communication systems, such as PSK, Quadrature Amplitude Modulation (QAM) and their deferentially-coherent variations, it is possible to change the modulation format in post-processing while keeping the originally transmitted signal into the water unchanged. This involves transforming the original coded modulation scheme into an alternative one through an offline combination of XOR and constellation dithering operations [27]. Specifically, applying binary XOR operations to the originally transmitted bits, alternative Forward Error Correction (FEC) codes can be accommodated. Furthermore, applying additive dithering to the original constellation, it becomes possible to support alternative constellations with the same, higher, or lower modulation order. To minimize the disparity between offline replay and real-life performance, the utilization of minimum-L_2-norm dithering is necessary.

Here, we revisit the technique of [27] and focus on replay systems that use constant modulus constellations, i.e., M-PSK or M-ary Differential PSK (M-DPSK). These constellations encompass a significant portion of the constellations employed in current UWA communication systems. We show that XOR operations can be substituted with phase shifts directly applied to the channel symbols without loss of channel replay optimality. For brevity of this discussion, we denote M_1 and M_2 positive integers describing the PSK modulation order of the replay symbols and the immutable transmitted symbols, respectively.

Fig. 1(a) shows the block diagram of the transmitter used for channel replay purposes. The gray-colored blocks within the diagram represent the elements of the transmitter used in a prior experiment and so they are immutable. During the experiment, the information source was mapped to a unique sequence of N complex-valued symbols, $\{g(n)\}_{n=1}^{N}$, where each symbol is drawn from the M_2-PSK constellation. The symbol $g(n)$ corresponds to $\log_2(M_2)$ bits and is transmitted during the nth symbol time interval, which spans a duration of T seconds. Additionally, N_p known (pilot) M_2-PSK symbols, independent of the information message and known to the receiver, are prepended to the N data symbols to reliably establish initial time and phase synchronization during receiver equalization. The synthesized baseband signal, $u(t)$, is expressed as

$$u(t) = \sum_{n=1}^{N+N_p} g(n)p(t - nT), \tag{1}$$

$$p(t) = \frac{\sin(\pi t/T)}{\pi t/T} \frac{\cos(\pi \beta t/T)}{1 - 4\beta^2 t^2/T^2}, \tag{2}$$

where $p(t)$ denotes the raised cosine pulse with roll-off β ([28], pp.529). At the last stage of the transmitter, $u(t)$ is shifted to passband by modulating the carrier f_c. The resulting passband signal, $x(t)$, occupies the bandwidth $[f_c - \frac{\beta}{2T}, f_c + \frac{\beta}{2T}]$ Hz. As the arrival time of $x(t)$ at the receiver can vary, a detection preamble is appended to $x(t)$ in order to facilitate coarse synchronization at the receiver. The detection preamble comprises a known pseudo-random ± 1 sequence that is modulated using the same pulse $p(t)$ as the data-bearing signal.

The white-colored blocks of Fig. 1(a) are the elements of the transmitter used for implementing the desired coded modulation scheme in channel replay mode. A message of n_b bits is encoded with a code with rate $r = n_b/n_c$ resulting in the generation of a codeword $c(i) \in \{0, 1\}_{i=1}^{n_c}$ comprising n_c bits. Note that the terms "codeword" and "packet" are used interchangeably in this context. Then, the codeword
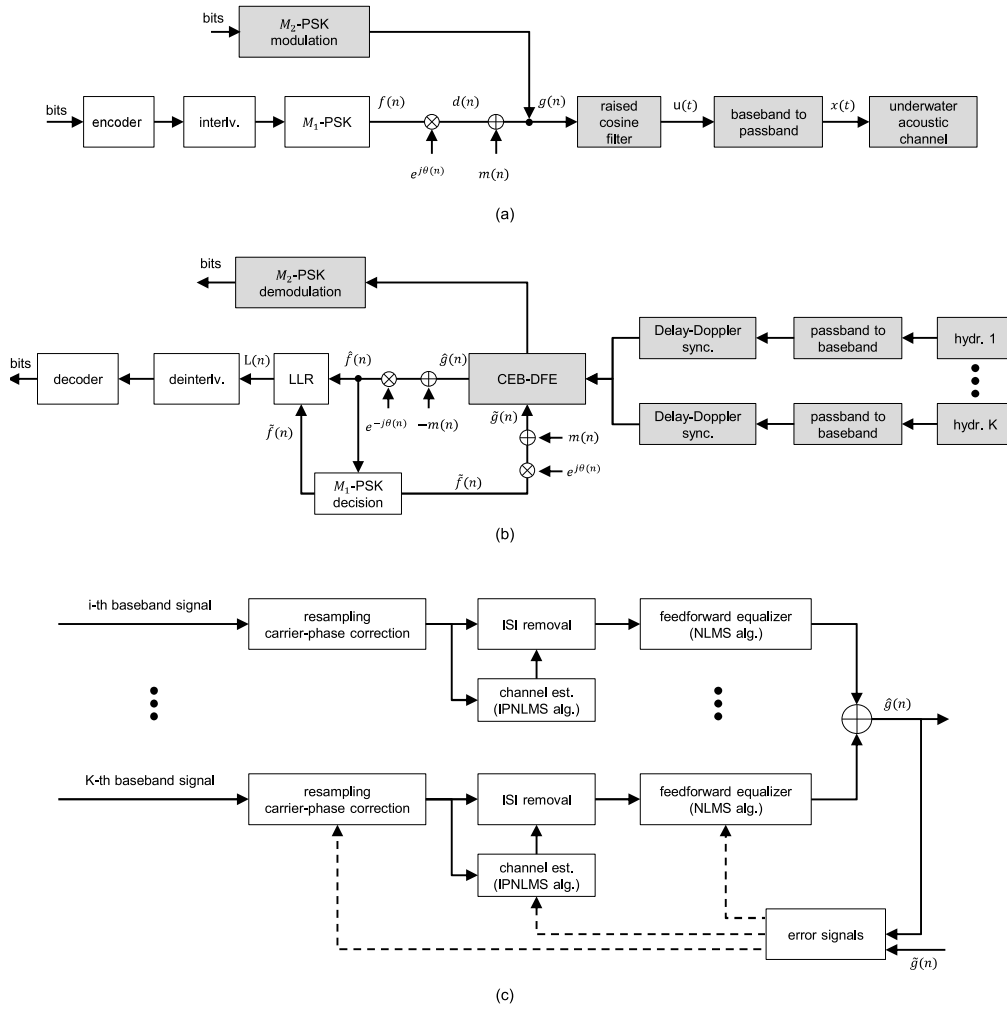
Fig. 1. (a) replay transmitter block diagram; (b) receiver block diagram; (c) CEB-DFE block diagram.

$\{c(i)\}_{i=1}^{n_c}$ undergoes interleaving (scrambling) with a predetermined order, following which a block of $\log_2(M_1)$ bits is mapped into one M_1-PSK channel symbol, producing a total number of $N_s = n_c/\log_2(M_1)$ symbols. This process is commonly referred to as BICM.[2] Let $f(n)$ be the symbol for transmission during the nth symbol time interval. Subsequently, $f(n)$ is mapped to $g(n)$, as follows:

$$d(n) = f(n)e^{j\theta(n)} \tag{3}$$

$$g(n) = m(n) + d(n), \tag{4}$$

where $d(n)$ is a proxy M_1-PSK symbol that is dictated by the transmitted $g(n)$ and the constellation dither $m(n)$. The phase $\theta(n)$ denotes the rotation $f(n)$ must undergo to align with $d(n)$. We stress that the number of replay symbols N_s must be equal or less than N, thereby imposing an upper limit on the number of information bits, n_b, as follows: $n_b \le N \cdot r \cdot \log_2(M_1)$.

The optimal dither sequence $\{m(n)\}_{n=1}^{N_s}$ must be of minimum L_2 norm, i.e., $\sum_{n=1}^{N_s} |m(n)|^2$, to prevent the amplification of Inter-symbol Interference (ISI) at the receiver due to dithering. To provide insight about $m(n)$ and its impact on $d(n)$, Figs. 2(a)–2(f) illustrate examples for $M_1, M_2 \in \{2, 4, 8\}$. In all figures, observe that $m(n)$ is well-balanced and has a mean of zero. When $g(n)$ belongs to the typical 2-PSK constellation $\{\pm 1\}$, the optimal dither causes $d(n)$ to assume values from

the constellation $\{e^{jk\pi/2+\pi/4}|k = 0, 1, 2, 3\}$ and $\{e^{jk\pi/4+\pi/8}|k = 0, \ldots, 7\}$, respectively, for $M_1 = 4$ and $M_1 = 8$. On the other hand, if $g(n)$ is associated with the typical 4-PSK set $\{e^{jk\pi/2}|k = 0, 1, 2, 3\}$, then $d(n)$ takes on values from the constellation $\{\pm e^{j\pi/4}\}$ for $M_1 = 2$. Similarly, when $g(n)$ belongs to the common 8-PSK set $\{e^{jk\pi/4}|k = 0, \ldots, 7\}$, then $d(n)$ assumes values from the constellation $\{\pm e^{j\pi/8}\}$ for $M_1 = 2$.

Since both symbols $d(n)$ and $f(n)$ belong to the M_1-PSK constellation, they are either equal or differ by a phase shift $\theta(n)$ at each n. It is straightforward to show that for $M_1 = 2$ the phase difference $\theta(n)$ takes on values from the set $\{0, \pi\}$. For $M_1 = 4$, $\theta(n)$ belongs to the set $\{0, \pm\pi/2, \pi\}$ while for $M_1 = 8$, $\theta(n)$ falls within $\{0, \pm\pi/4, \pm\pi/2, \pm 3\pi/4, \pi\}$. We emphasize that $\theta(n)$ and $m(n)$ are known to the receiver as part of the replay process. The linear mapping described in Eqs. (3)–(4) ensures optimal channel replay, as guaranteed by the findings in [27].

Fig. 1(b) illustrates the block diagram of the receiver. The gray-colored blocks represent the components of the receiver that remain constant during the channel replay process. The processing begins by down-converting the received time series at each hydrophone to baseband, followed by the application of a low-pass filter to suppress out-of-band noise. Following this, the wideband cross-ambiguity function between the transmitted and received preamble signal is computed independently for each hydrophone series. This function estimates the delays and motion-induced time scales of multipath arrivals. The time scale of the strongest multipath arrival is used as reference to resample the subsequent data signal and offset its coarse time scaling. Lastly, the K data signals, after being downsampled at a rate of four samples

---

[2] If TCM is desired, the interleaver is positioned after symbol mapping. The block diagram is omitted for brevity.
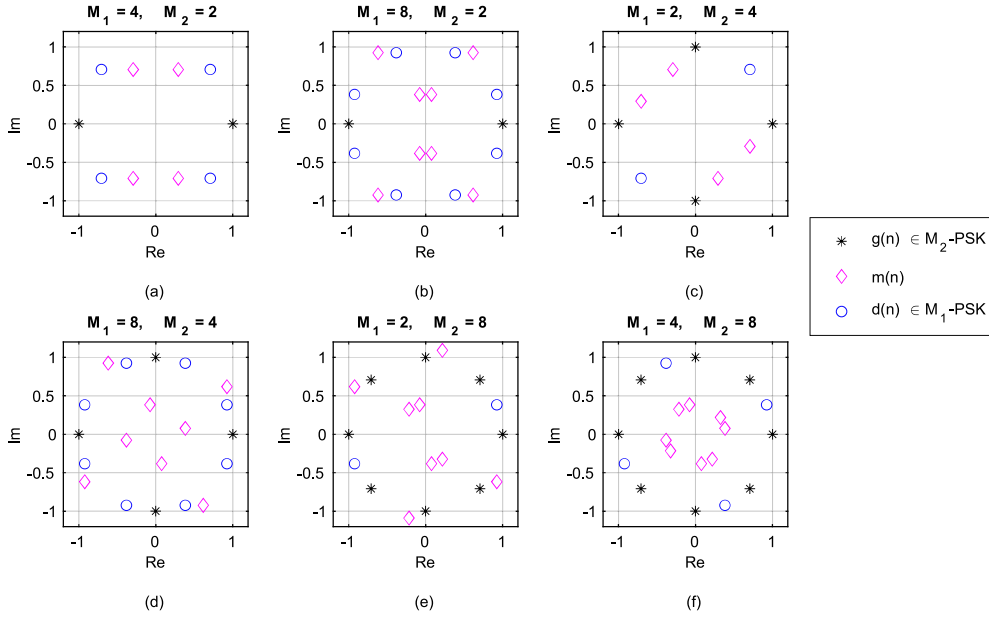
Fig. 2. (a)–(f): complex-valued point constellations for $m(n)$, $d(n) \in M_1$-PSK and $g(n) \in M_2$-PSK. At each symbol period n, $m(n)$, $d(n)$, $g(n)$ become a distinct point in their respective constellations.

per symbol, are fed into a channel-estimate-based Decision Feedback Equalizer (CEB-DFE).

The detailed signal processing steps of the Channel-Estimate-Based Decision Feedback Equalizer (CEB-DFE) can be found in previous works such as [9,29]. Yet, to provide a comprehensive picture, we briefly describe the CEB-DFE operations here. The CEB-DFE begins with a training phase spanning N_p symbol periods. Post this training, it transitions to decision-directed mode for the subsequent N_s symbol periods, yielding the sequence $\{\hat{g}(n)\}_{n=1}^{N_s}$ that represents the estimated channel symbols. The components of the CEB-DFE are illustrated in Fig. 1(c), whose filter coefficients undergo adjustments at each symbol interval, all aiming to minimize channel-induced ISI. The operations kick off with fine-scale symbol synchronization. A Phase-Locked Loop (PLL) of the first order deduces the time scale for the nth symbol interval at each hydrophone. This is achieved by processing phase shifts from previously transmitted pilot symbols during training mode or decided data symbols in decision-directed mode. The deduced time scale then guides a linear interpolation filter, enabling the kth signal's resampling at two samples per symbol. Subsequently, K received signal samples across the K hydrophones combined with past data or pilot symbols generate K channel impulse response estimates. The Improved-Proportionate Normalized Least Mean Squares (IPNLMS) algorithm is used for channel estimation. This algorithm, known for its fast channel tracking, exploits the sparse multipath structure encountered in each of the K acoustic links. Furthermore, the IPNLMS algorithm is advantageous due to its low memory requirements and linear computational complexity relative to the number of channel coefficients. With knowledge of the channel responses and the previously transmitted symbols (pilots or decisions), the ISI is synthesized and subtracted from the K received signals. Finally, each ISI-compensated signal is passed through a linear transversal filter and all K outputs are added to deduce the symbol estimate $\hat{g}(n)$. The coefficients of the K transversal filters are jointly adapted using a Normalized Least Mean Squares (NLMS) algorithm, which is based on a mean squared error cost function, exhibiting linear computational complexity concerning filter tap count. It is important to note that the implementation of the CEB-DFE, as described, does not necessitate knowledge of the spatial geometry of the array.

The channel replay components of the receiver, denoted by the white blocks in Fig. 1(b), leverage the sequence $\{\hat{g}(n)\}_{n=1}^{N_s}$ to retrieve the originally transmitted codeword (or packet). Specifically, each

individual $\hat{g}(n)$ undergoes a mapping to yield $\hat{f}(n)$, achieved through the linear transformation: $\hat{f}(n) = e^{-j\theta(n)}(\hat{g}(n)-m(n))$. This transformation results in the sequence $\{\hat{f}(n)\}_{n=1}^{N_s}$, which is subsequently converted into a series of log-likelihood ratios (LLRs), symbolized as $\{L(c(i))\}_{i=1}^{n_c}$. The LLR sequence corresponds to the series of transmitted coded bits $\{c(i)\}_{i=1}^{n_c}$ and provides a measure of how likely each received bit is a logical one or logical zero.

For the specific case of $M_1 = 2$, whereas each coded bit $c(i)$ is mapped into a 2-PSK channel symbol $f(n)$ ($n_c = N_s$), each $L(c(i))$ (or $L(c(n))$) is computed as follows [30]:

$$\sigma^2(n) = \frac{1}{N_p + n} \sum_{m=1}^{N_p+n} \left| \tilde{f}(m) - \hat{f}(m) \right|^2, \tag{5}$$

$$L(c(n)) = -\frac{1}{\sigma^2(n)} \left(\left| \tilde{f}(n) - \hat{f}(n) \right|^2 - \left| -\tilde{f}(n) - \hat{f}(n) \right|^2 \right), \tag{6}$$

where $\tilde{f}(n)$ denotes the closest constellation point of $\hat{f}(n)$ and $\sigma^2(n)$ represents the estimate of the noise power at the output of the CEB-DFE up to time n. It is important to note that when incorrect decisions are present, i.e., $\tilde{f}(n) \neq f(n)$, the estimated value of $\sigma^2(n)$ will be underestimated.

Finally, the sequence $\{L(c(i))\}_{i=1}^{n_c}$ is rearranged (deinterleaved) to match the original order of the encoder. This reordered sequence is then relayed to the decoder, which discerns the transmitted n_b-bit message.

3. Channel codes

Future High-North communication systems are envisioned to service long-range links with battery-powered unmanned underwater vehicles. A receiver based on the DFE faces the challenge of channel tracking and mitigating ISI under low Signal-to-Noise Ratio (SNR) conditions. Hence, the adoption of 2-PSK modulation ($M_1 = 2$) is preferable over higher order PSK due to its robustness to channel estimation errors and its effectiveness to reduce erroneous feedback in the DFE structure [31].

The combination of an (n_c, n_b) encoder with 2-PSK modulation yields a channel symbol sequence of length n_c. Consequently, the choice of n_c becomes crucial as larger values allow for the correction of more bit errors at the cost of lower data rates and increased hardware complexity in terms of processing time and memory requirements. Here, we choose to investigate codeword lengths ranging from a few hundred bits to a couple of thousand bits, aligning with established

practices in UWA communication systems. Notable examples include the use of 144-bit codewords in the JANUS physical layer [32], 512-bit codewords in the NILUS physical layer [33], and 2048-bit codewords in the Sweep-Spread-Carrier (S2C) modem described in [34].

In this work, we employ several prominent coding theory methods. From the block code family, we incorporate BCH, TBC, LDPC, and polar codes, while from the convolutional code family, we utilize convolutional and turbo codes. Our aim is to compare the considered codes under an equal code rate constraint. While decoding complexity is an important consideration, it is not a performance metric that we focus on in this work. In the subsequent sections, we provide an overview of the key characteristics of the selected channel codes.

3.1. BCH codes

BCH codes [35] (Chapter 3) are popular in both communications (e.g., the DVB-S2 digital television standard) and data storage systems (e.g., CDs and flash drives) due to their ability to achieve numerous code rates and error-correcting capabilities. A notable feature of BCH codes is their precise control over the number of symbol errors that can be corrected. During the encoding process, the $n_c - n_b$ parity bits are generated by dividing the message polynomial, representing the message bits, by a specific generator polynomial. Efficient hard (algebraic) decoding is achieved through the computation of syndromes and the error location polynomial using the Berlekamp–Massey algorithm. The computational complexity of this algorithm is approximated as $O(n_c \log(n_c))$.

In our study, we consider two specific BCH codes: BCH(511,103) with a code rate of approximately 0.2, capable of correcting up to 61 errors, and BCH(2047,1024) with a code rate of 0.5, capable of correcting up to 106 errors.

3.2. TPCs

TPCs [36] offer flexibility in terms of codeword size and code rate, making them suitable for various standards, including the IEEE 802.16 (WiMAX). The encoder is constructed by sequentially applying two linear block codes to a message arranged in a matrix format. The first block code is applied row by row, while the second block code is applied column by column to the row-encoded data. The decoder achieves near-optimum decoding through the Chase-Pyndiah algorithm, which consists of two stages: a "Chase" type hard-decision (based on Hamming distance) decoding stage followed by an LLR-based decoding stage (Pyndiah decoding). The complexity of the Chase-Pyndiah algorithm can be represented as $O(I \cdot n_c \cdot 2^{2t})$, where I denotes the number of iterations and t represents the number of least reliable bit positions of the received codeword considered in the Chase decoding stage.

In our study, we employ two TPC codes: TPC(640,128) with a code rate of approximately 0.2, constructed by serially applying BCH(255,239) and BCH(63,51), followed by appropriate message shortening; TPC(1728,1024) with a code rate of approximately 0.6, constructed by applying BCH(128,120) twice, followed by appropriate message shortening. For both TPC decoders, we consider up to ten iterations ($I \leq 10$).

3.3. LDPC codes

LDPC codes [37] are highly regarded for their ability to approach the capacity of the Additive White Gaussian Noise (AWGN) channel through low-complexity iterative probabilistic decoding. Due to their demonstration in providing low BER at high data rates, LDPC codes are used in various standards including the uplink/downlink shared channel of the Fifth Generation (5G) New Radio (NR) standard. The LDPC encoder is defined based on a sparse parity-check matrix and the optimal decoder uses the belief propagation algorithm, which iteratively updates the bit LLRs until all parity checks are satisfied or

a maximum number of iterations is reached. The complexity of LDPC decoding is generally proportional to the number of ones in the parity-check matrix resulting in approximately linear complexity with respect to the length of the code, i.e., $O(n_c)$.

In this paper, we use the LDPC implementation of the 3rd Generation Partnership Project (3GPP) [38]. The LDPC encoding in 3GPP's 5G New Radio (NR) standard has a base code rate of 0.5. To achieve different code rates, certain coded bits may be punctured (omitted) or repeated accordingly. Below, we investigate two LDPC codes: LDPC(640,128) with a code rate of $r = 0.2$ and LDPC(2048,1024) with a code rate of $r = 0.5$. Additionally, we perform up to ten decoding iterations to evaluate the performance of the LDPC decoders.

3.4. Polar codes

Polar codes [39] are a relatively recent addition to the family of error correction codes and have garnered significant attention in the field of coding theory due to their remarkable theoretical properties. The adoption of polar codes in uplink/downlink control channel of 5G NR is a notable milestone because it is the first time that polar codes have been used in a commercial standard. The polar encoder leverages on the idea of *channel polarization*, i.e., a transformation process to construct codewords with binary channels that either become highly reliable (nearly noiseless) or highly unreliable (very noisy). Hence, in the encoding process, the source bits are sent over the reliable channels, while the unreliable channels are either left unused or used to transmit known (frozen) bits. Efficient decoding of short codewords is achieved via Cyclic Redundancy Check (CRC)-aided Successive Cancellation (SC) with a list [40]. Essentially, the encoder is combined with a CRC code, which acts as an outer code. The decoder initially uses the received LLRs to generate a list of candidate transmitted bit sequences and then, it computes the CRC value for each candidate sequence and checks it against the received CRC value. If the computed CRC matches the received one, the candidate is deemed to be the correct codeword, and the decoding process is terminated early. The decoding complexity is on the order of $O(n_c \cdot L)$, L being the list size.

In this paper, we use the 3GPP polar implementation as detailed in [41]. Specifically, two polar codes are employed: polar(640,128) with $r = 0.2$ and polar(2048,1024) with $r = 0.5$. Given the desired codeword length and code rate, the reliability sequence that determines the reliable bit-channels that should carry information bits is computed. Furthermore, the chosen CRC and list size is, respectively, 11 bits and $L = 40$.

3.5. Convolutional codes

Convolutional codes [28] (Chapter 8) are widely used in many wireless communication standards such as the GCM and CDMA2000 cellular standard. In UWA communications, a notable application of convolutional codes is at the physical layer of the JANUS standard [32]. During the encoding process, the input bits pass through a shift register that performs several modulo-2 additions at the output. The number of bits stored in the shift register, k, determines the *constraint length* of the code. The decoder searches for the most likely transmitted codeword via the Viterbi algorithm, which uses the received LLRs to compute branch metrics. The algorithm's complexity is primarily determined by the constraint length of the code and is approximately proportional to 2^{k-1}.

In this study, we consider two types of codes: conv(640,128) with generator polynomial [257 233 323 271 357], $k = 9$ and $r = 0.2$; conv(2048,1024) with generator polynomial [21675 27123], $k = 13$ and $r = 0.5$. The Viterbi traceback length is set to $\frac{2.5(k-1)}{1-r}$ and the traceback path starts at the state with the best metric and ends in the all-zero state.
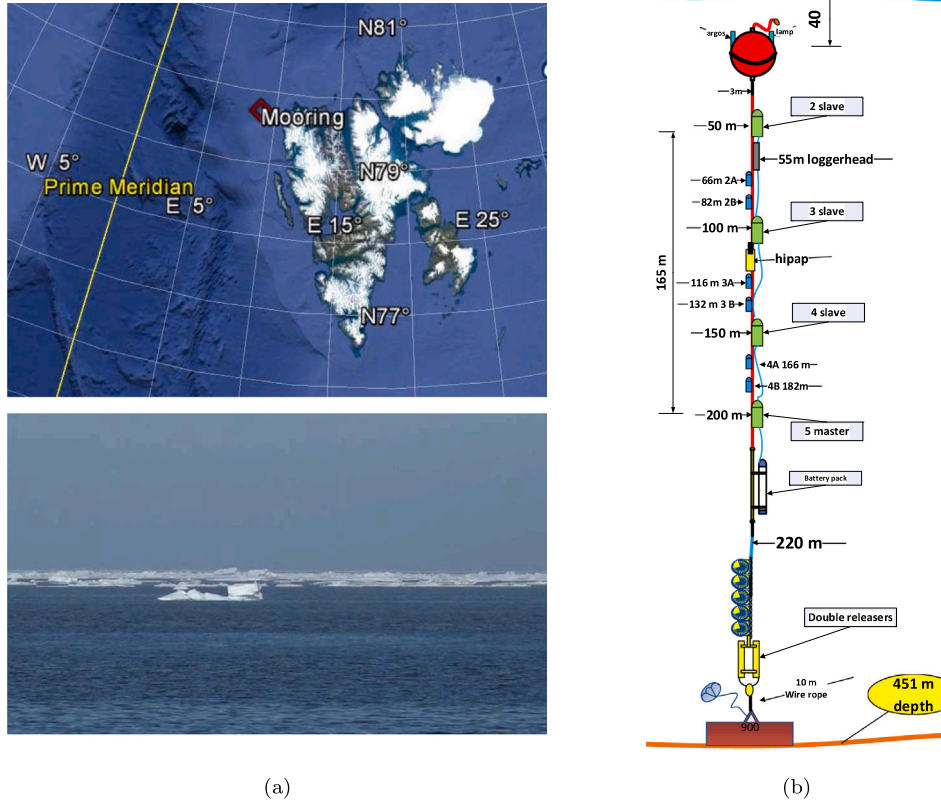
Fig. 3. (a) map of experimental area (top) and sea surface picture (bottom). The red marker indicates the position of the acoustic mooring. (b) Acoustic mooring design.

3.6. Turbo codes

Turbo codes [42] are used in the Universal Mobile Telecommunications System (UMTS) standard and also as part of the Fourth Generation (4G) long-term evolution (LTE) standard. A turbo encoder is typically composed by a parallel concatenation of two convolutional codes separated by an interleaver. The interleaver permutes the bits between the encoders, which helps to break up any correlations in the input data and thus improve the performance of the code. The turbo decoder consists of two a-posterior probability (APP) decoders [43], which exchange extrinsic LLR information via the interleaver and deinterleaver for a fixed number of iterations. The turbo decoding complexity is directly proportional to the codeword length, the number of iterations and the state size of the constituent convolutional encoders.

In this paper, we use the 3GPP turbo implementation as detailed in [44], which consists of two recursive systematic convolutional encoders with $k = 4$. The base code rate is $1/3$, and depending on the needed rate, certain coded bits may be punctured (omitted) or repeated to match the desired code rate. Furthermore, two turbo codes are considered: turbo(640,128) with $r = 0.2$ and turbo(2048,1024) with $r = 0.5$. The interleaver size is selected based on the desired n_b. Additionally, we perform up to ten decoding iterations to evaluate the performance of the turbo decoders.

4. NREP'21 sea trial

4.1. Area and experimental setup

The Nordic Recognized Environmental Picture 2021 (NREP'21) sea trial was organized by the Centre for Maritime Research and Experimentation (CMRE) and took place in the Yermak Plateau, located northwest of the Svalbard Islands, in June 2021. A primary objective of the trial was to assess the performance of communication signals for different link ranges. The transmissions occurred during two specific time slots: from 21:55 to 22:25 Coordinated Universal Time (UTC) on June 23rd, and from 02:15 to 02:35 UTC on June 24th. All received signals were captured using a hydrophone array. Fig. 3(a) depicts the map of the experimental area, with the red marker indicating the position of the receiver. Additionally, Fig. 3(a) shows a picture of the sea surface within the operational area, where ice floes can be observed. It is worth noting that moving ice floes occasionally passed over the established links, as evidenced by the results discussed below. The sound source used in the experiment was deployed off the vessel NRV Alliance, and its source level was set to 160 dB re 1 μPa re 1 m. The ship was freely drifting at speeds ranging from 0.5 to 1 m/s, resulting in fluctuating source depths between 132 and 135 meters due to vessel motion.

Fig. 3(b) illustrates the bottom-mounted mooring that hosted the receiving hydrophone array. Its deployment position was at 79° 44.116' N, 8° 50.333' E and the bathymetry in the area was relatively flat with a depth of about 456 m. Ten hydrophones were attached to the mooring at depths of 50 m, 66 m, 82 m, 100 m, 116 m, 132 m, 150 m, 166 m, 182 m and 200 m. In addition, four depth sensors were mounted at 50 m, 100 m, 150 m, and 200 m. After processing the depth measurements, we find that the mooring remained in its original designed depth except during the period 22:30 (June 23rd)–01:30 (June 24th) where the entire structure gradually submerged deeper by 5 m.

The spectrogram of the transmitted audio waveform is illustrated in Fig. 4. The arrangement of the six signals within the audio are as follows: a 2-PSK-based preamble, a 2-PSK-based data signal, another 2-PSK-based preamble, a 4-PSK-based data signal, a third 2-PSK-based preamble, and finally, an 8-PSK-based data signal. All data signals carry the same number of channel symbols, that is 20200 symbols. The role of the preamble signal is to provide coarse synchronization of its subsequent data signal as well as estimate the channel impulse response. The
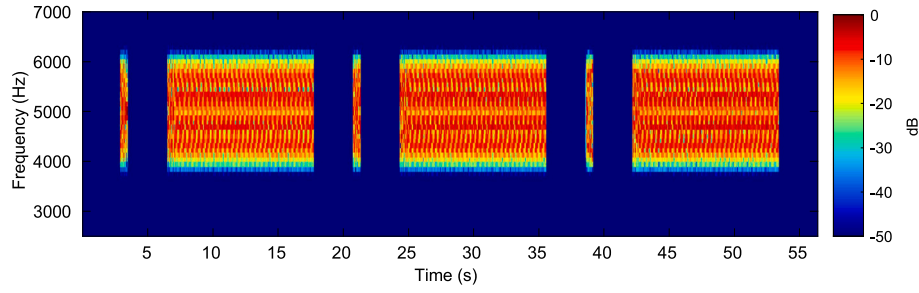
Fig. 4. The spectrogram of the transmitted waveform. The intensity refers to the power in decibel scale and is normalized to unity (0 dB).
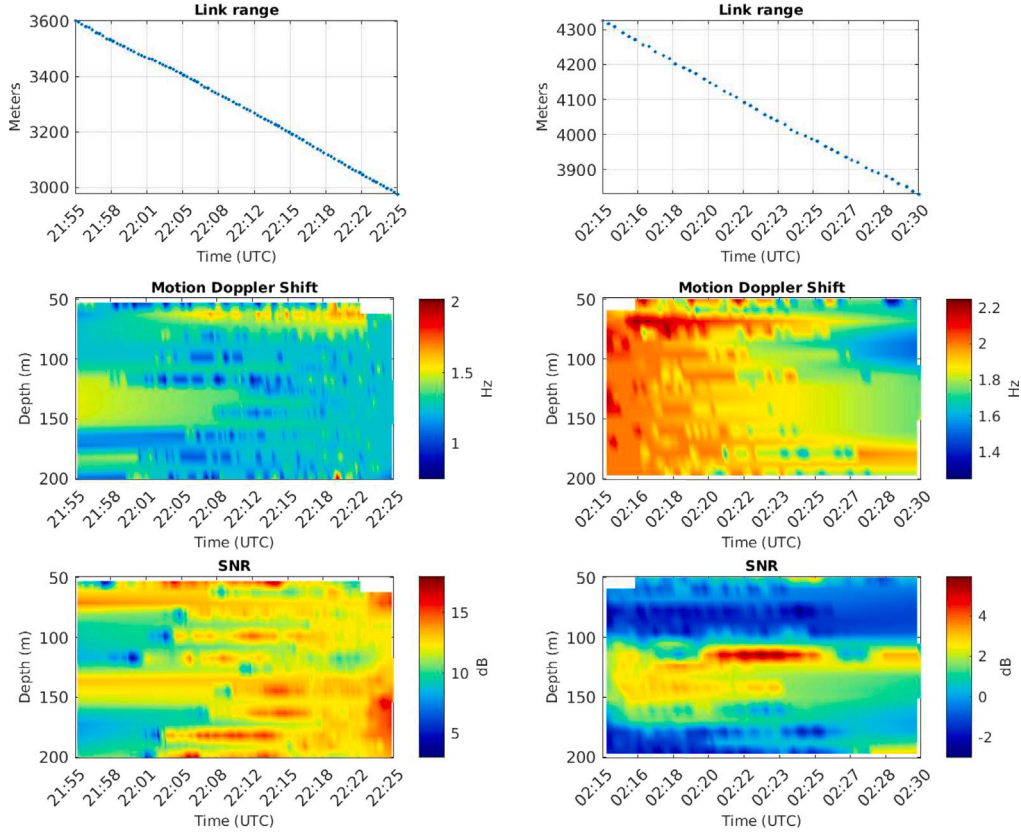

Fig. 5. First row: link range vs. time. Second row: Doppler Shift vs. depth and time. Third row: SNR vs. depth and time. The plots are distinguished between June 23rd (left side) and June 24th (right side).

duration of the data signal and the preamble is approximately 11.3 s and 0.6 s, respectively. Their bandwidth, within the range of 3830–6170 Hz, is established by the parameters of the raised cosine filter: specifically, a roll-off factor of $\beta = 0.3$, a symbol duration of $T = 1/1800$ seconds, and a carrier frequency $f_c = 5000$ Hz.

4.2. Acoustic channel characteristics

It is instructive to present the range separation between the ship and the acoustic mooring during the course of the experiment. This separation is tied to specific acoustic channel characteristics, e.g., SNR, motion-induced Doppler and multipath delay profile. These characteristics significantly impact communications performance and are analyzed separately for the two transmission intervals of June 23rd and June 24th.

The upper part of Fig. 5 shows the evolution of the link range between the ship and the acoustic mooring during the two transmission intervals. The left side of the plot corresponds to June 23rd, while the right side corresponds to June 24th. The link range is computed using the GPS logs of the ship and the known position of the mooring. It is worth noting that on June 23rd, the signal transmissions from NRV Alliance started at a distance of 3.65 km from the mooring. As the ship drifted due to sea currents, the distance decreased to 3.04 km, where the transmissions ceased. On June 24th, NRV Alliance initiated transmissions at a range of 4.35 km and concluded at a range of 3.85 km from the mooring.

Additionally, the middle part of Fig. 5 illustrates the motion-induced Doppler shift as a function of depth and time. This plot is generated by computing the wideband cross-ambiguity function of the received preamble at each of the ten hydrophones and estimating the Doppler shift corresponding to the strongest multipath arrival. Doppler values at adjacent depths and received times are computed via interpolation. The observed variation in Doppler shift result from the dynamic geometry between the ship and the mooring, coupled with the encountered sound speed profile. This sound speed profile achieved its nadir proximal to the ocean surface, followed by a rapid increment to approximately 1465 m/s at a depth of 50 m. Beyond the 50 meter depth, the sound speed oscillated within the 1460–1467 m/s range. Refer to [26] for a
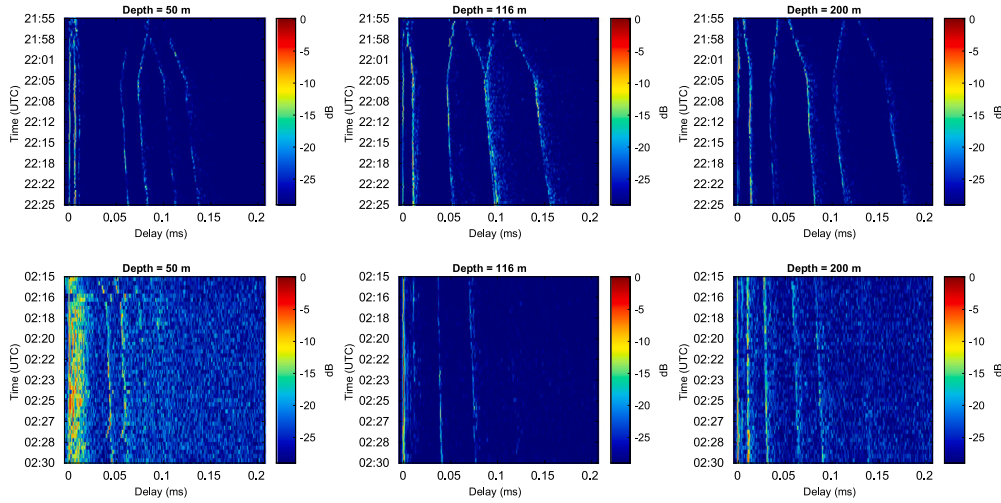
Fig. 6. Baseband impulse response estimates for three distinct depths: 50 m, 116 m and 200 m. In all plots, the *x*-axis shows multipath delay, the *y*-axis shows absolute time, and the intensity refers to the amplitude in decibel scale. The first and second row correspond to the first and second transmission slot, respectively.

plot of the measured sound speed profile. It is important to note that the Doppler shift values are exclusively positive, as the ship consistently sailed towards the mooring during the transmissions. During the first transmission slot, the Doppler shift ranged from 0.8 Hz to 1.6 Hz, while during the second slot, it ranged from 1.4 Hz to 2.2 Hz. To provide insight, a 2-Hz-Doppler shift of a 5 kHz carrier corresponds to about 0.5 m/s rate of reduction of the line-of-sight path, which is consistent with the ship motion.

Furthermore, the lower part of Fig. 5 presents the SNR as a function of depth and time. The SNR computation is performed by splitting the hydrophone time series into two segments: one segment contains the preamble signal masked with noise while the other segment contains only noise. The SNR is calculated as a power ratio: $\text{SNR} \approx 10 \cdot \log_{10}(P_{\text{signal+noise}}/P_{\text{noise}} - 1)$. It is clearly seen that the SNR exhibits random fluctuations in both depth and time due to the time-varying link geometry and the non-isotropic ambient noise. During the first transmission slot, the SNR varies between 5 dB and 17 dB, while during the second slot, where the exercised ranges are longer, the SNR varies between −4 dB and 5 dB. The substantial variability in SNR across depth presents a compelling proposition for exploring the combination of signals from multiple hydrophones for the purpose of data demodulation.

Fig. 6 shows the time evolution of the amplitude of the estimated baseband impulse response for three hydrophone depths: 50 m, 116 m and 200 m. The first and second row correspond to the first and second transmission slot, respectively. The estimated impulse response is obtained by translating the received preamble signal in baseband, low-pass filtering and correlating it with the transmitted pseudo-noise sequence, with compensation for motion-induced Doppler distortion. For each depth and transmission slot, the maximum response amplitude is normalized to unity (0 dB). In all plots, the intensity at the delay of 0 ms corresponds to the fastest sound ray connecting the transmitter and the receiver. In most cases, the fastest arrival corresponds to the line-of-sight path but there are exceptions. For example, at a depth of 50 m, the fastest arrival corresponds to the surface bounce. The maximum delay spread, defined as the time difference between the slowest and fastest arrival, is about 170 ms observed in the first slot and at a depth of 200 m. For this delay spread, the ISI for a single-carrier communication system extends to 306 symbol intervals, which is challenging for data demodulation with a single hydrophone. It is worth mentioning that during the second transmission the arrivals appearing around 0 ms observed at a depth of 50 m are attributed to scattering off moving ice floes. This observation is justified by the findings presented in Fig. 7.

The upper part of Fig. 7 shows the sound ray tracing plots for two specific link geometries based on the measured sound speed profile. The difference between the two geometries lies solely in the receiver depth: on the left side the receiver is at 50 m while on the right side the receiver is at 200 m. Furthermore, the transmitter's position corresponds to the ship's latitude/longitude at 02:25:06 (UTC) on June 24th. Although the presence of ice floes between the ship and the mooring is confirmed by the ship's radar, we stress that these plots are generated via BELLHOP [45], assuming a flat sea surface without ice floes. The ray tracing indicates that the receiver at 50 m encounters no line-of-sight path but the fastest arrival undergoes a single surface reflection. Conversely, the receiver at 200 m experiences a line-of-sight signal path. In the lower part of Fig. 7, the ray tracing output is convoluted with the autocorrelation of the preamble signal (matched filter) to synthesize the baseband impulse response for each geometry. It should be noted that the transmitting hardware frequency response is not incorporated in this process. Furthermore, the measured impulse responses are overlaid with the simulated responses, facilitating a visual comparison between empirical observations and simulations. For the receiver scenario at 200 meters depth, the synthesized response aligns well with the measured impulse response in terms of delay times, successfully predicting the sea surface bounce at 11.7 ms, the bottom bounce at 30.3 ms, and the surface-bottom bounce at 63.7 ms. However, the discrepancy in amplitude between measured and simulated responses is attributed to the crude resolution of the waveguide boundaries given that the wavelength is about 30 cm at $f_c = 5000$ Hz. For the receiver at 50 m depth, BELLHOP accurately predicts the bottom bounce delay at 43 ms and the surface-bottom bounce delay at 57 ms. Nevertheless, a clear divergence between measured and synthesized impulse responses is evident near the 0 ms delay. While BELLHOP anticipates a regular specular reflection, the actual surface bounce path experiences scattering off ice floes located approximately 3.2 km from the transmitter. It is postulated that in the absence of ice floes, the measured response would also showcase a specular reflection, similar to the condition witnessed at the 200-m receiver depth.

5. Results

The primary objective of this section is to evaluate and rank the performance of the six examined codes based on their PER, defined as the ratio of successfully decoded packets to the total number of received packets. A packet is considered unsuccessfully received if it contains at least one erroneous bit. To maintain consistency, we leverage data from the NREP'21 sea trial, integrating it with the replay framework
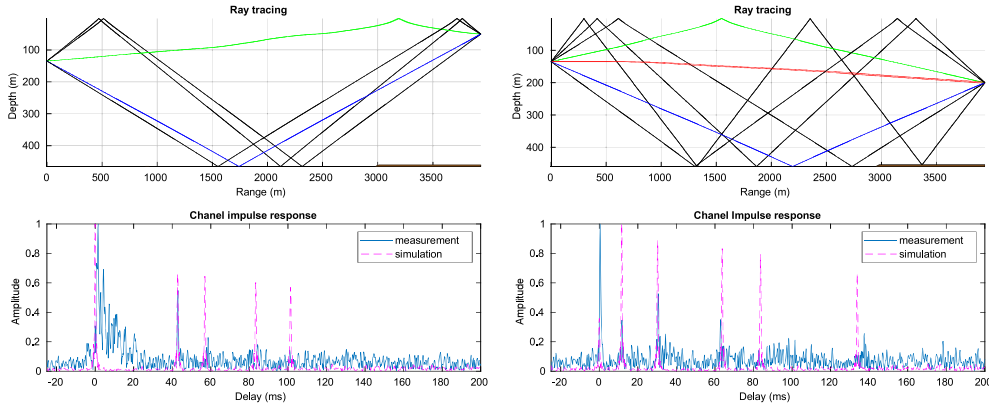
Fig. 7. Ray tracing-based and measured channel impulse responses at 50 m (left) and 200 m (right).

discussed in Section 2. This guarantees performance assessment under identical channel conditions. Our evaluation distinguishes between two packet lengths: short and long. The standard length for short packets across most coding schemes is 128 bits, with the exception of the BCH scheme, which uses 103 bits. All these schemes encode their short packets at a 0.2 code rate. On the other hand, long packets have a standard length of 1024 bits and are encoded at a 0.5 rate. TPC is an outlier, operating at a 0.6 rate. It is worth noting that these short packets are common for operational tasks like command and control or updating underwater node statuses. Meanwhile, the long packets are well-suited for transmitting sensor data.

Our results are separated into four scenarios depending on the number of hydrophones used in the CEB-DFE. The aim is to understand the relationship between performance improvement and the increase in hydrophone number, implying a corresponding rise in equipment cost. In the first scenario, the CEB-DFE uses data from a single hydrophone to decode each transmitted packet. Hence, each transmitted packet is decoded up to ten times, if it is detected in all hydrophones, before the PER is computed. This procedure ensures that all channels encountered by the specific packet are factored into the computation. In the second scenario, the CEB-DFE combines signals from two hydrophones to decode each transmitted packet. Accounting for all different hydrophone combinations, each packet is decoded at most $\binom{10}{2} = 45$ times for computing its PER. Should a probe signal be undetectable in either of the two selected hydrophones, that specific combination is exempted from the PER computation. In the third scenario, we consider a three-channel CEB-DFE, leading to a scenario where each packet is decoded up to 120 times, reflecting all $\binom{10}{3} = 120$ hydrophone combinations. Lastly, in the fourth scenario, an eight-channel CEB-DFE is considered, applied to all $\binom{10}{8} = 45$ hydrophone combinations. The cumulative number of processed packets, short and long, for each scenario is summarized in Table 1.

In addition, Table 1 lists the filter lengths employed for channel estimation (via IPNLMS filter) and equalization (using the NLMS filter) across the four scenarios discussed. Although the analysis performed in this study was carried out in Matlab, these filter lengths provide insight into the computational complexity and memory requirements a real-time system might demand to execute CEB-DFE in a similar environment. It is important to stress that both IPNLMS and NLMS algorithms require linear computational complexity in relation to their respective filter lengths. In the current implementation, the IPNLMS filter spans the entire multipath delay spread observed by each hydrophone. On the other hand, the NLMS filter is designed to cover a range of ± 10 ms centered on the fastest signal arrival for a single hydrophone. However, as the number of hydrophones increases, the effective span per hydrophone of NLMS gradually decreases. This reduction stems from the NLMS algorithm's reduced efficiency in channel

tracking as the filter length grows - a challenge that the IPNLMS algorithm addresses more effectively, thanks to its capability to leverage channel sparseness.

In Fig. 8, we detail the PER for the six evaluated codes. Among them, the polar code stands out, exhibiting the lowest PER across all packet lengths and hydrophone combinations. As expected, the code yields lower PER for the short packet than the long one since the short packet is encoded with a lower code rate. Specifically, for $k = 128$ bits, the PER results for the polar code are as follows: $0.15, 0.047, 0.012$, and $1.3 \cdot 10^{-5}$ for configurations with one, two, three, and eight hydrophones, respectively. The disparity in PER between single and eight hydrophone setups is strikingly pronounced. The second best performance after the polar is achieved by the convolutional code for the short packet. Yet, the performance improvement of the polar relative to the convolutional is substantial, namely, $22\%, 34\%, 54\%, 98\%$, for one, two, three, eight hydrophones, respectively. When considering packets of length $k = 1024$ bits, the polar achieves a PER of $0.31, 0.19, 0.11$, and 0.015, for one, two, three, and eight hydrophones, respectively. For the long packet, the turbo codes achieves the second best performance after the polar. Nevertheless, the dominance of the polar code remains significant manifesting performance improvement of $27\%, 26\%, 28\%$, and 39% for the same hydrophone configurations.
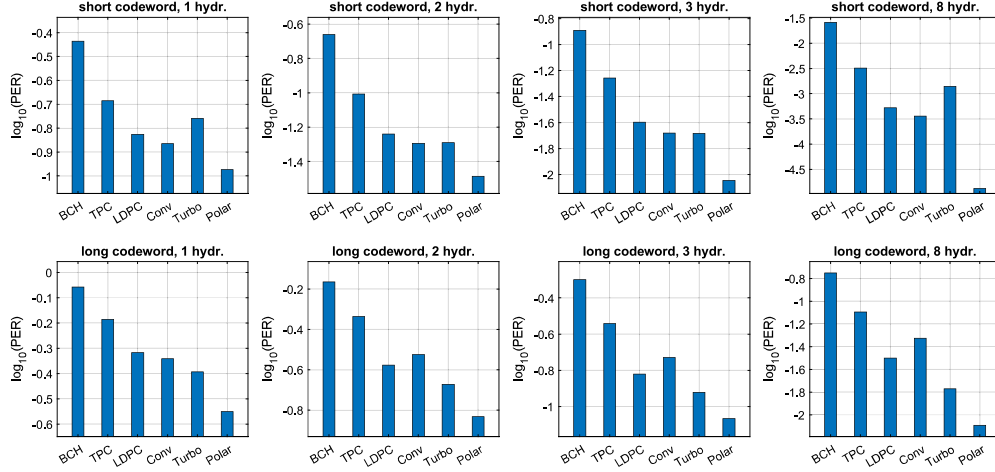
In the above analysis, the CEB-DFE operates independently from the decoder. It is known that the DFE performance degrades when wrong past symbol decisions enter into the feedback loop. This naturally raises the inquiry: would the implementation of turbo equalization in lieu of standard equalization provide a substantial reduction of the PER? The distinct advantage of turbo equalization is its ability to iteratively exchange bit likelihoods between the equalizer and decoder, thereby mitigating the impacts of incorrect feedback [46]. In our approximation of turbo equalization, the CEB-DFE is employed solely in its training mode. This means that correct past symbols are provided to the feedback loop for the ongoing symbol estimation. The output symbol sequence is then transferred to the decoder, mirroring the standard operational mode of Fig. 1(c). Hence, the obtained PER can be considered as a lower bound of a genuine iterative structure between CEB-DFE and the decoder. The work in [46] has demonstrated that this bound becomes tight to the actual turbo performance after eight iterations for moderate-to-high SNR channels.

In Fig. 9, we detail the PER decrease of the turbo-like CEB-DFE-decoder structure relative to its traditional counterpart across all different scenarios. A consistent observation is that the most marked enhancement is realized in the polar-driven communication system, irrespective of packet lengths and hydrophone configurations. Specifically, for the short packet, the PER decrease for the polar-driven turbo-like system is $27\%, 30\%$, and 26% for one, two, and three hydrophones, respectively. Remarkably, with an eight-hydrophone setup, both the conventional and turbo-like system exhibit identical PERs

Table 1

CEB-DFE filter lengths and number of processed packets for different number of input hydrophones.

Num. of hydrophones	IPNLMS filter length (taps)	NLMS filter length (taps)	Num. of received short packets	Num. of received long packets
1	720	73	11 200	4200
2	1440	90	37 596	12 532
3	2160	135	99 984	33 328
8	5760	136	74 628	18 657

Fig. 8. PER evaluation of considered codes for varied number of packet lengths and hydrophones.
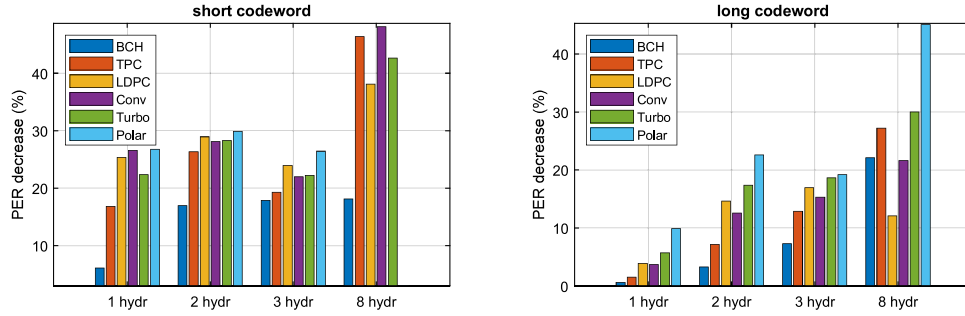
Fig. 9. Evaluation of PER decrease between CEB-DFE-decoder with turbo equalization property and traditional CEB-DFE-decoder.
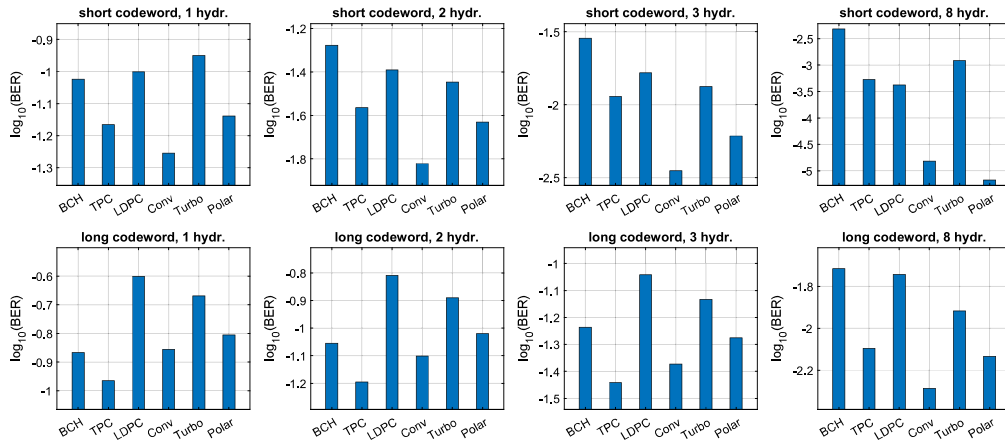
Fig. 10. BER evaluation for varied number of code rates and hydrophones.

(there is no bar in the plot). For the long packet, the polar-based turbo-like system yields a PER improvement of 10%, 23%, 19%, and 45% for one, two, three and eight hydrophones, respectively. Consequently, we may argue that a polar-centric turbo equalizer offers a substantial edge over the traditional polar-centric equalizer.

Finally, Fig. 10 shows the BER analysis for the six considered codes. The BER is computed as the average number of information bit flips after decoding. Notably, the trends in the BER findings diverge from those observed in the PER results in Fig. 8. No single code consistently achieves the optimal BER performance; this metric fluctuates based on

the coding rate and the hydrophone setup within the CEB-DFE. For example, the convolutional code shows the lowest BER for 0.2 code rate with 1-3 hydrophone configurations. In addition, the convolutional code shows the lowest BER for 0.5 code rate and eight hydrophone configurations. Conversely, the TPC shows the lowest BER for 0.6 code rate with 1-3 hydrophone configurations. The polar code's BER performance is not stellar, but there is a reason: when the polar decoder makes an error, especially in high SNR scenarios, it is not typically a single random bit-flip. Instead, it can often be a structural error, i.e., a failure of the decoder to correctly understand the transmitted codeword structure resulting in a burst of bit errors. This contrasts with codes like LDPC or turbo, where mistakes are generally sporadic due to their iterative decoding methods and unique parity-check matrix structures. Nevertheless, we stress that the PER results above offer a clearer understanding of the most suitable channel code for our goals. They encompass end-to-end system performance, factoring in packet size and interleaving. When evaluating higher-layer protocols, the PER provides valuable insights into necessary packet retransmissions and ensuing latency.

6. Conclusions

This paper evaluated the error performance of six major FEC codes prevalent in the communications literature: convolutional, turbo, LDPC, BCH, TPC, and polar. The basis for this assessment was a set of signals previously recorded in an underwater acoustic (UWA) experiment conducted northwest of the Svalbard Islands. While not initially intended for FEC comparison, these signals employed 2/4/8-PSK modulation and were captured in the 3830–6170 Hz frequency band using a linear hydrophone array. This UWA environment presented unique challenges, such as diffuse multipath propagation due to sound scattering off ice floes, Doppler distortion caused by platform movement, and variable SNR. Using the constellation dithering technique, we formulated a channel replay framework that incorporated an encoder, 2-PSK modulation, multi-channel CEB-DFE and a decoder. We examined two packet configurations: a short packet with a 128-bit payload encoded at a rate of 0.2, and a longer 1024-bit packet encoded at a rate of 0.5. For the short packet, the polar code demonstrated superior performance and its PER advantage over the second-best (convolutional code) increased from 22% to 98% as the number of hydrophones expanded from one to eight. In the case of the long packet, the PER advantage of the polar code over the second-best (turbo code) showed a steady improvement from 27% to 39% after increasing the number of hydrophones. Additionally, we found that augmenting the CEB-DFE-polar-decoder with a turbo equalization property resulted in a significant PER reduction of 10%–45%, relative to the conventional CEB-DFE-polar-decoder, as the hydrophone count increased. These results are particularly noteworthy as they suggest that the polar code could lead to substantial power savings at the transmitter, given its reduced need for retransmissions.

The findings of this study are closely linked to the specific design of the transceiver and the distinct characteristics of the High North environment. In future research, we plan to use signals transmitted in various oceanic regions and utilize the same channel replay framework to investigate the broader applicability of our results.

CRediT authorship contribution statement

Konstantinos Pelekanakis: Conceptualization, Formal analysis, Investigation, Methodology, Writing – original draft, Writing – review & editing. **Pietro Paglierani:** Conceptualization, Writing – review & editing. **Alberto Alvarez:** Funding acquisition, Writing – review & editing. **João Alves:** Funding acquisition, Writing – review & editing.

Declaration of competing interest

The authors declare that they have no known competing financial interests or personal relationships that could have appeared to influence the work reported in this paper.

Data availability

Data will be made available on request. Rules and conditions apply.

References

[1] A. Song, M. Stojanovic, M. Chitre, Editorial underwater acoustic communications: Where we stand and what is next? IEEE J. Ocean. Eng. 44 (1) (2019) 1–6.
[2] Intergovernmental Panel on Climate Change, Fifth assessment report, 2014, https://www.ipcc.ch/report/ar5/syr/.
[3] M. Wang, J.E. Overland, A sea ice free summer Arctic within 30 years? Geophys. Res. Lett. 36 (7) (2009) 1–5.
[4] T.W. Haine, B. Curry, R. Gerdes, E. Hansen, M. Karcher, C. Lee, B. Rudels, G. Spreen, L. de Steur, K.D. Stewart, R. Woodgate, Arctic freshwater export: Status, mechanisms, and prospects, Glob. Planet. Change 125 (2015) 13–35.
[5] M.-L. Timmermans, S.R. Jayne, The arctic ocean spices up, J. Phys. Oceanogr. 46 (4) (2016) 1277–1284.
[6] J.F. Lynch, G.G. Gawarkiewicz, Y.-T. Lin, T.F. Duda, A.E. Newhall, Impacts of ocean warming on acoustic propagation over continental shelf and slope regions, Oceanography 31 (2) (2018) 174–181.
[7] A. Alvarez, A model for the arctic mixed layer circulation under a summer-time lead: implications for the near-surface temperature maximum formation, Cryosphere 17 (8) (2023) 3343–3361.
[8] L. Freitag, K. Ball, J. Partan, P. Koski, S. Singh, Long range acoustic communications and navigation in the Arctic, in: OCEANS 2015 - MTS/IEEE, Washington, USA, 2015, pp. 1–5.
[9] K. Pelekanakis, S. Blouin, D. Green, Performance analysis of underwater acoustic communications in barrow strait, IEEE J. Ocean. Eng. 46 (4) (2021) 1438–1449.
[10] P. van Walree, D. Tollefsen, V. Forsmo, Under-ice acoustic communication in the Nansen Basin, in: 2021 Fifth Underwater Communications and Networking Conference (UComms), Lerici, Italy, 2021, pp. 1–5.
[11] M. Barbeau, S. Blouin, A. Traboulsi, Performance of an underwater communication system in a sea trial done in the Canadian arctic, in: IEEE International Mediterranean Conference on Communications and Networking (MeditCom), Athens, Greece, 2021, pp. 448–453.
[12] L. Freitag, P. Koski, A. Morozov, S. Singh, J. Partan, Acoustic communications and navigation under Arctic ice, in: 2012 Oceans, in: 2012 Oceans, Hampton Roads, VA, USA, 2012, pp. 1–8.
[13] H.C. Song, P.N. Mikhalevsky, A.B. Baggeroer, Transarctic acoustic telemetry, J. Acoust. Soc. Am. 136 (4) (2014) 1491–1494.
[14] L. Freitag, P. Koski, S. Singh, T. Maksym, H. Singh, Acoustic communications under shallow shore-fast Arctic Ice, in: OCEANS 2017, Anchorage, AK, USA, ISBN: 978-0-6929-4690-9, 2017, pp. 1–5.
[15] P. van Walree, H. Buen, D. Tollefsen, Under-ice and open-water acoustic communication in the Fram Strait, in: OCEANS 2019, Marseille, France, 2019, pp. 1–5.
[16] J. Trubuil, A. Goalic, N. Beuzelin, An overview of channel coding for underwater acoustic communications, in: MILCOM 2012 - 2012 IEEE Military Communications Conference, Orlando, FL, USA, 2012, pp. 1–7.
[17] J. Kim, Y.-H. Cho, H. Ko, T. Im, Performance comparison of short-length error-correcting codes in an underwater OFDM systems, in: 2019 International Conference on Information and Communication Technology Convergence, ICTC, Jeju, Korea (South), 2019, pp. 121–123.
[18] S. Roy, T. Duman, V. McDonald, J. Proakis, High-rate communication for underwater acoustic channels using multiple transmitters and space-time coding: Receiver structures and experimental results, IEEE J. Ocean. Eng. 32 (3) (2007) 663–688.
[19] P. van Walree, G. Leus, Robust underwater telemetry with adaptive Turbo multiband equalization, IEEE J. Ocean. Eng. 34 (4) (2009) 645–655.
[20] I. Karasalo, T. Öberg, B. Nilsson, S. Ivansson, A single-carrier Turbo-coded system for underwater communications, IEEE J. Ocean. Eng. 38 (4) (2013) 666–677.
[21] J. Huang, S. Zhou, P. Willett, Nonbinary LDPC coding for multicarrier underwater acoustic communication, IEEE J. Sel. Areas Commun. 26 (9) (2008) 1684–1696.
[22] A. Rafati, H. Lou, C. Xiao, Peer-reviewed technical communication, soft-decision feedback Turbo equalization for LDPC-coded MIMO underwater acoustic communications, IEEE J. Ocean. Eng. 39 (1) (2014) 90–99.
[23] V. Lidstrom, Evaluation of polar-coded noncoherent acoustic underwater communication, IEEE J. Ocean. Eng. PP (99) (2023) 1–14.
[24] Y. Zhai, J. Li, H. Feng, F. Hong, Application research of polar coded OFDM underwater acoustic communications, EURASIP J. Wireless Commun. Networking 2023 (1) (2023) 26.

[25] K. Pelekanakis, A.B. Baggeroer, Exploiting space–time–frequency diversity with MIMO-OFDM for underwater acoustic communications, IEEE J. Ocean. Eng. 36 (4) (2011) 502–513.

[26] K. Pelekanakis, A. Alvarez, J. Alves, Comparison of coded modulation for short messages over high north underwater acoustic channels, in: WUWNet '22: Proceedings of the 16th International Conference on Underwater Networks & Systems, Association for Computing Machinery, Boston, MA, USA, 2022, pp. 1–8.

[27] S. Yang, G.B. Deane, J.C. Preisig, N.C. Sevuktekin, J.W. Choi, A.C. Singer, On the reusability of postexperimental field data for underwater acoustic communications R&D, IEEE J. Ocean. Eng. 44 (4) (2019) 912–931.

[28] J.G. Proakis, Digital Communications, fourth ed., McGraw-Hill, Boston, 2000.

[29] K. Pelekanakis, M. Chitre, New sparse adaptive algorithms based on the natural gradient and the L_0-norm, IEEE J. Ocean. Eng. 38 (2) (2013) 323–332.

[30] A. Viterbi, An intuitive justification and a simplified implementation of the MAP decoder for convolutional codes, IEEE J. Sel. Areas Commun. 16 (2) (1998) 260–264.

[31] M. Stojanovic, J.G. Proakis, J.A. Catipovic, Analysis of the impact of channel estimation errors on the performance of a decision-feedback equalizer in fading multipath channels, IEEE Trans. Commun. 43 (2/3/4) (1995) 877–886.

[32] J. Alves, T. Furfaro, K. LePage, A. Munafò, K. Pelekanakis, R. Petroccia, G. Zappa, Moving JANUS forward: A look into the future of underwater communications interoperability, in: OCEANS 2016 MTS/IEEE, Monterey, CA, USA, 2016, pp. 1–6.

[33] H.S. Dol, P. Casari, T. van der Zwan, R. Otnes, Software-defined underwater acoustic modems: Historical review and the NILUS approach, IEEE J. Ocean. Eng. 42 (3) (2017) 722–737.

[34] K.G. Kebkal, A.K. Kebkal, O.G. Kebkal, R. Bannasch, Modelling and validation of basic characteristics in underwater acoustic sweep-spread-carrier communications, in: 2015 IEEE Underwater Technology, UT, Chennai, India, 2015, pp. 1–9.

[35] R.H. Morelos-Zaragoza, The Art of Error Correcting Coding, second ed., John Wiley & Sons, Hoboken, NJ, USA, 2006.

[36] H. Mukhtar, A. Al-Dweik, A. Shami, Turbo product codes: Applications, challenges, and future directions, IEEE Commun. Surv. Tutor. 18 (4) (2016) 3052–3069.

[37] D.J. MacKay, R.M. Neal, Near Shannon limit performance of low density parity check codes, Electron. Lett. 32 (18) (1996) 1645–1646.

[38] R. Maunder, Ldpc-3gpp-matlab, 2023, GitHub repository, https://github.com/robmaunder/ldpc-3gpp-matlab/releases/tag/v1.0.

[39] E. Arikan, Channel polarization: A method for constructing capacity-achieving codes for symmetric binary-input memoryless channels, IEEE Trans. Inform. Theory 55 (7) (2009) 3051–3073.

[40] A. Balatsoukas-Stimming, M.B. Parizi, A. Burg, LLR-based successive cancellation list decoding of polar codes, IEEE Trans. Signal Process. 63 (19) (2015) 5165–5179.

[41] R. Maunder, Polar-3gpp-matlab, 2023, GitHub repository, https://github.com/robmaunder/polar-3gpp-matlab/releases/tag/v1.0.

[42] C. Berrou, A. Glavieux, P. Thitimajshima, Near Shannon limit error-correcting coding and decoding: Turbo-codes (1), in: Proceedings of ICC '93 - IEEE International Conference on Communications, 2, Geneva, Switzerland, 1993, pp. 1064–1070 vol.2.

[43] S. Benedetto, D. Divsalar, G. Montorsi, F. Pollara, A Soft-Input Soft-Output Maximum A Posterior (MAP) Module to Decode Parallel and Serial Concatenated Codes, Tech. rep., 42–127, Jet Propulsion Laboratory, California Institute of Technology, 1996, pp. 22–24.

[44] R. Maunder, Turbo-3gpp-matlab, 2023, GitHub repository, https://github.com/robmaunder/turbo-3gpp-matlab/releases/tag/v1.0.

[45] M.B. Porter, H.P. Bucker, Gaussian beam tracing for computing ocean acoustic fields, J. Acoust. Soc. Am. (ISSN: 0001-4966) 82 (4) (1987) 1349–1359.

[46] E.M. Sozer, Reliable Communications over Frequency-Selective Rapidly-Fading Channels, Thesis (Ph.D.), Northeastern University, Boston, USA, 2003.

Award for Best Paper in Radar, Sonar & Navigation. Dr. Pelekanakis, served as the secretary and vice chairman for the IEEE Oceanic Engineering Society (OES) Singapore chapter in 2013 and 2014, respectively. He has been with the organizing committee of IEEE UComms since 2016. He is currently a member of the IEEE OES Administrative Committee and also serves as an Associate Editor for the IEEE Journal of Oceanic Engineering. Dr. Pelekanakis is an IEEE Senior Member.

Pietro Paglierani received the master's and Ph.D. degrees in electronic engineering from the University of Padua, Italy. He is currently a Scientist at the NATO's Science and Technology Organization (STO)-Centre for Maritime Research and Experimentation, La Spezia, Italy. His main research interests focus on digital signal processing, in particular on underwater acoustic communications and secure communications in underwater networks. Previously, he was with Italtel S.p.A, Milan, where he was the Team Leader of the Digital Signal Processing Group at the Research and Development Unit, Tektronix, Necsy S.p.A, and Consorzio Padova Ricerche, where he was a Designer of signal processing applications and algorithms for telecommunications.

Alberto Alvarez received the M.S. degree in physics from the University of Santiago de Compostela, Santiago de Compostela, Spain, in 1991, a first Ph.D. degree from the Physics Department, University of Balearic Island, Balearic Island, Spain, in 1995, the second Ph.D. degree in underwater robotics from the Department of Electrical Engineering, University of Pisa, Pisa, Italy, in 2004, and a third PhD degree in ocean engineering and marine technology from the Polytechnic University of Madrid, Madrid, Spain, in 2015. Professionally, he was an Assistant Professor with the University of Balearic Island from 1995 to 1997. He received a postdoctoral position with the Physics Department, National Central University, Jhongli City, Taiwan, from 1997 to 1999, to work in underwater acoustics. From 1999 to 2002, he joined the Department of Rapid Environmental Assessment (REA) at SACLANT Undersea Research Centre, La Spezia, Italy, as a Scientist. Since 2002, he has been a Senior Scientist in the Spanish National Council Research (CSIC). From 2008 to 2016, he got a special leave from CSIC to join the Department of Systems and Technology of the NATO Undersea Research Centre (former SACLANT Undersea Research Centre) as a Senior Scientist. His research focused on the application of underwater gliders to Rapid Environmental Assessment-REA. He joined the Centre for Maritime Research and Experimentation (former NATO Undersea Research Centre) in 2019 as a Principal Scientist and Programme Manager of the Programme Environmental Knowledge and Operational Effectiveness. His current research interest is focused on REA methodologies in the Arctic Ocean. Scientific contributions can be reviewed at https://orcid.org/0000-0001-6583-8515.

João Alves received the B.Sc. and M.Sc. degrees in electrotechnical engineering, control and robotics from the Technical University of Lisbon, Lisbon, Portugal, in 1996 and 2005, respectively. He has been working in underwater robotics and associated technologies since 1995. He had a key role in the development of the hardware and software architectures for the MARIUS autonomous underwater vehicle and DELFIM autonomous surface vessel, developed at the Technical University of Lisbon. In 2003 he co-founded a private start-up company—Blue Edge Systems Engineering offering services and conducting R&D activity in the maritime domain. In 2007, he took scientific leadership for the underwater communications activities of the EC project GREX where pioneering maritime cooperative robotics was demonstrated. In late 2009, he joined the NATO Undersea Research Centre, now Centre For Maritime Research and Experimentation (CMRE), as a Scientist to work on underwater communications. He led studies in support of establishing the first underwater communications standard and developed innovative protocols for underwater ad hoc networking. In 2014, he took a leadership role as a Principal Scientist responsible for the underwater communications activities with CMRE. He conducted several trials as a Scientist-in-Charge, leading teams of several people during long sea-going campaigns. In 2019, he took leadership of a wide programmatic area of CMRE for interoperability and security of maritime unmanned systems. Mr. Alves is the Co-General Chair for the IEEE OES UComms conference. He is a Guest Editor for the IEEE Journal of Oceanic Engineering and an Area Editor for the Elsevier's Journal of Ad Hoc Networks. He was the recipient of the NATO Scientific Achievement Award 2018 for his work as one of the team leaders in the development and promulgation of JANUS, the first digital underwater communications standard.

Konstantinos Pelekanakis received his Diploma from the Department of Electronic and Computer Engineering, Technical University of Crete, Greece, in 2001 and his M.Sc. and Ph.D. degrees in Mechanical and Ocean Engineering from the Massachusetts Institute of Technology (MIT), Cambridge, USA, in 2004 and 2009, respectively. From 2009 to 2015, he worked with the Acoustic Research Laboratory at the National University of Singapore as a Research Fellow. From 2015 to 2023, he was a Senior Scientist at the NATO Centre for Maritime Research and Experimentation (CMRE) in La Spezia, Italy. He is currently a Senior Scientist at the Netherlands Organisation for Applied Scientific Research (TNO) in the Hague, the Netherlands. In 2001, he was awarded the MIT Presidential Fellowship and in 2018, he was the co-recipient of the NATO Scientific Achievement Award. In 2019, he was the co-recipient of the IET Premium